Lab on a Chip

PAPER

View Article Online
View Journal

Cite this: DOI: 10.1039/d0lc00538j

Deterministic droplet coding *via* acoustofluidics†

Peiran Zhang,‡[a] Wei Wang, ‡[ab] Hai Fu,[ac] Joseph Rich, [d] Xingyu Su, [a] Hunter Bachman,[a] Jianping Xia, [a] Jinxin Zhang,[a] Shuaiguo Zhao,[a] Jia Zhou*[b] and Tony Jun Huang *[ad]

Received 25th May 2020,
Accepted 19th October 2020

DOI: 10.1039/d0lc00538j

rsc.li/loc

Droplet microfluidics has become an indispensable tool for biomedical research and lab-on-a-chip applications owing to its unprecedented throughput, precision, and cost-effectiveness. Although droplets can be generated and screened in a high-throughput manner, the inability to label the inordinate amounts of droplets hinders identifying the individual droplets after generation. Herein, we demonstrate an acoustofluidic platform that enables on-demand, real-time dispensing, and deterministic coding of droplets based on their volumes. By dynamically splitting the aqueous flow using an oil jet triggered by focused traveling surface acoustic waves, a sequence of droplets with deterministic volumes can be continuously dispensed at a throughput of 100 Hz. These sequences encode barcoding information through the combination of various droplet lengths. As a proof-of-concept, we encoded droplet sequences into end-to-end packages (*e.g.*, a series of 50 droplets), which consisted of an address barcode with binary volumetric combinations and a sample package with consistent volumes for hosting analytes. This acoustofluidics-based, deterministic droplet coding technique enables the tagging of droplets with high capacity and high error-tolerance, and can potentially benefit various applications involving single cell phenotyping and multiplexed screening.

Introduction

Multiplexed assays in microfluidic systems involve batch processing (*e.g.*, production, storage, screening, and actuation) of a large number of micro-scale fluids containing various analytes in a high-throughput manner.[1] Recently, droplet microfluidics has become a powerful toolset in biomedical engineering and lab-on-a-chip based applications owing to its unprecedented throughput, high precision, low reagent consumption rate, and cost-effectiveness. Various applications, involving single cell-cultivation,[2,3] compound screening,[4–6] and emulsion PCR,[7,8] have utilized micro-droplets as micro-beakers to host independent reactions. Currently, although droplets can be generated, screened, and sorted in a high-throughput manner, the real-time identification and tracking of individual droplets is still challenging, limiting the potential of micro-droplets as individually addressable micro-reactors in the aforementioned applications. This challenge is primarily due to the inability to uniquely tag colossal amounts of droplets with labels that can be easily extracted and decoded on-chip. Thus, a barcoding technique that can uniquely label and identify every individual droplet (*i.e.*, assigning unique identifiers to individual droplets following a specific algorithm) with low system complexity, low error-rate, and high encoding capacity is desired.

To date, various micro-barcoding techniques have been developed to tag and identify individual analytes (*e.g.*, particles, cells, droplets) in a high-throughput manner.[9–12] Theoretically, any type of signal that can be detected and differentiated is applicable in synthesizing barcodes. A straightforward strategy utilized in micro-barcoding applications is to directly mimic commercial barcodes by embedding data into micro-scale geometric patterns.[13–15] Although this strategy guarantees simple decoding using microscopic images, the synthesis of barcode microstructures requires sophisticated procedures (*e.g.*, lithography or micro-printing in micro- or nano-scale) or requires extra chemical additives, which can interfere with bio-analytes. To partially address the limitations above, combinatorial dyes,[16–19] fluorescence-generating nanostructures,[20–28] and non-linear scattering signals[29–32] have been introduced for facile droplet barcoding and decoding. The fluorescence/optical barcoding strategies hold unique advantages such as simple

[a] *Department of Mechanical Engineering and Material Science, Duke University, Durham, NC 27708, USA. E-mail: tony.huang@duke.edu*
[b] *ASIC and System State Key Laboratory, School of Microelectronics, Fudan University, Shanghai 200433, P. R. China. E-mail: jia.zhou@fudan.edu.cn*
[c] *Department of Fluid Control and Automation, School of Mechanics Engineering, Harbin Institute of Technology, Harbin, Heilongjiang 150000, P. R. China*
[d] *Department of Biomedical Engineering, Duke University, Durham, NC 27708, USA*
† Electronic supplementary information (ESI) available. See DOI: 10.1039/d0lc00538j
‡ These authors contribute equally to this work.

deployment and biocompatibility with bioanalytes inside the droplets. However, the limited choices of candidate materials and the spectral overlapping effects limit their barcoding capacity and decoding accuracy. Oligo-nucleotides[33–37] have also been employed for droplet barcoding, yet they generally can only reveal the encoded information until being amplified and sequenced.

As an alternative solution for droplet coding, the control of the size and spatial arrangements of droplets can add another dimension of control to the barcoding process without introducing any extra labels that may interfere with bio-analytes. However, this type of droplet barcoding has not been explored in microfluidic systems. Typical microfluidic droplet generation structures (*e.g.*, using glass capillaries,[38,39] T-junction,[40–42] or flow-focusing geometries[43–46]) do not allow for on-demand regulation of the size of a droplet. Recently, surface acoustic wave (SAW) based platforms have gained growing interests in a variety of research fields, including particle manipulation,[47–50] cell/vesicle separation,[51–54] model organism rotation,[55] and droplet manipulation,[56–65] due to its contact-free manner, high precision, high versatility, high biocompatibility, and compact device configuration.[66] For example, a device based on standing SAWs[58] has demonstrated the capability to continuously regulate the size of dispensed droplets by creating localized pressure gradients on the liquid interface. These pressure gradients trigger instabilities within the continuous two-phase flow to form droplets. However, the on-demand regulation of the size of every individual dispensed droplet has not been realized yet. Using focused travelling SAW beams at the orifice of a T-junction structure, the on-demand generation of droplets with controllable volumes was achieved.[61,64] Despite the advantages of currently developed platforms, size and spatial droplet coding function has yet been demonstrated and other concerns, such as high-power exposure or electro-chemical reactions, may arise due to the low acoustic attenuation of water.

Herein, we demonstrate an acoustofluidic mechanism that enables real-time size control of dispensed droplets and the deterministic coding of trains of droplets based on their spatial arrangement. The water flow was dynamically split with oil jets induced by a sequence of traveling surface acoustic wave (TSAW) bursts, which can be programmed in the time-domain. As such, a sequence of droplets with pre-determined volumes can be continuously dispensed with barcoding information embedded into their spatial arrangement. As a proof-of-concept demonstration, we encoded droplet sequences into end-to-end droplet packages (*e.g.*, 50 droplets per package). Each package consists of several address droplets arrayed in a binary volumetric combination of droplets. The address droplets with binary volume combinations serve as the unique barcoding tags, while the sample droplets are independent micro-beakers for hosting micro-reactions. Thus, the individual droplet can be visually identified by decoding the binary package address and counting the sequence number within the corresponding sample packages. The maximum capacity of this droplet coding algorithm is determined by the number of address bit droplets (*i.e.*, bits of the package address code) and the number of sample bit droplets in one package, which can simply be expanded or reduced by programming different TSAW intervals. Experiments have been carried out for the dependence of droplet dispensing performance on operational parameters such as flow rates and time intervals between adjacent TSAW pulses. This acoustofluidics-based deterministic droplet coding technique enables accurate, label-free, and real-time tagging of massive droplets with remarkable encoding capacity. It can potentially benefit various lab-on-a-chip applications including single cell-cultivation, compound screening, drug screening, and emulsion PCR.

Results

Working principle

As shown in Fig. 1a, a FIDT is placed adjacent to an oil chamber that has a circular sector geometry. Once the FIDT is excited by an alternating current (AC) signal, the generated TSAWs propagate in the predesigned direction and focus at the orifice of the oil chamber (*i.e.*, the geometrical focal point of the FIDT). During this process, the TSAWs travel along the interface of liquid and substrate, leak into the oil, and finally induce acoustic streaming and oil jets (Fig. 1b) in the oil chamber that travel towards the orifice. The speed of the oil jet is gradually accelerated, squeezed out at the orifice, and splits the continuous water flow to form a water droplet in the downstream of the T-junction (Fig. 1c and ESI† Note S1). The time-lapsed simulation of on-demand droplet splitting is shown in Fig. S1.†

The successful splitting of water droplets from the main flow relies on the combined effect of oil jets and surface tension, suggesting that the water channel should not be too wide to avoid laminar flows between the water flow and the transient oil jet. The size of orifice was mainly determined by the robustness of the oil–water interface to ensure no water will overflow to the oil channel while allowing the transient oil jet to pass with minimally allowed flow resistance. Overall, the main considerations for choosing the dimensions of the droplet coding unit are to allow the transient oil jets to gain higher speed before reaching the orifice while avoiding potential laminar flows between oil and water when SAW is on.

For a sequence of TSAW pulses, the water flow will be cut into a series of droplets of pre-determined volumes separated by the oil jets with tunable frequency (Movie S1–S3†). Given that the excitation signal and the resulting TSAW pulses can be well controlled, we can achieve robust size regulation of each droplet, suggesting that coding information into the spatial arrangement of droplets with different sizes is possible.

The droplet arrangement in Fig. 1a provides a schematic of the barcoding protocol by dispensing droplets successively

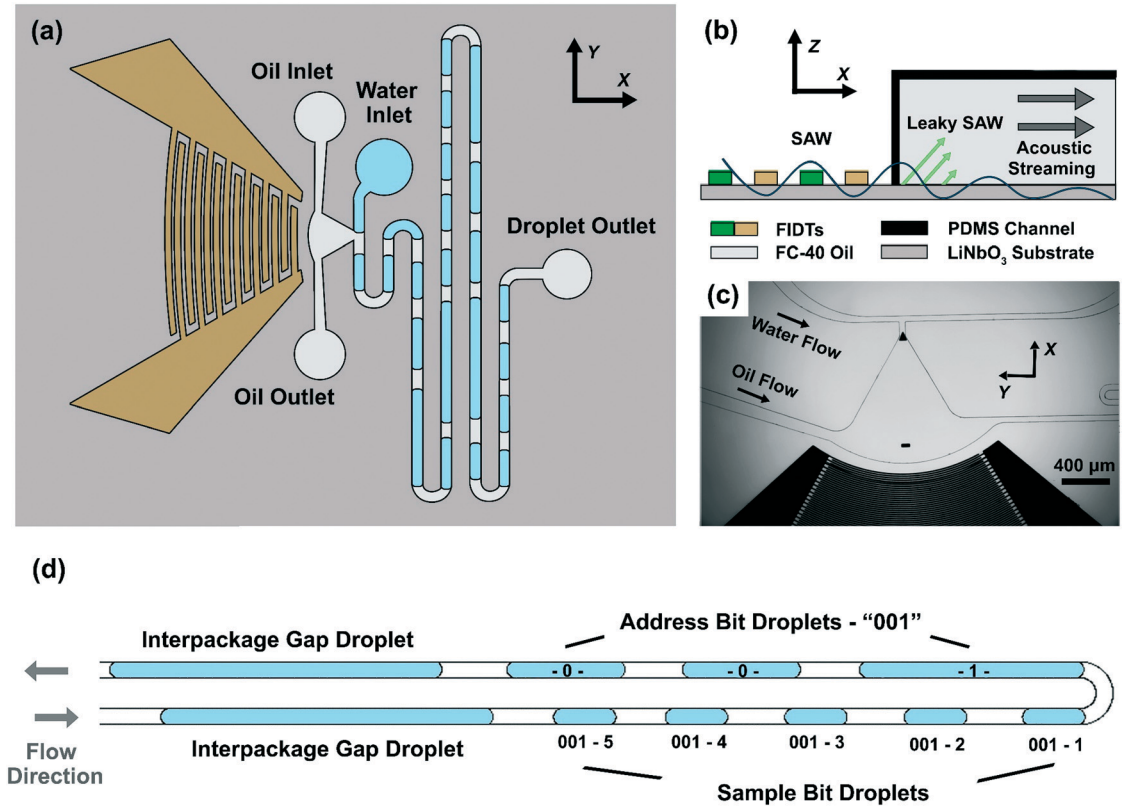

Fig. 1 Schematic of the acoustofluidic droplet dispensing and coding platform. (a) Oil in the chamber of a circular sector shape is jetted *via* the orifice upon the acoustic attenuation of the focused surface acoustic waves (SAWs). The oil jet cuts the continuous water flow to form dispersed droplets which flow downstream the microchannel. The size of droplets can be regulated in real-time by tuning the gap period between adjacent SAW pulses. (b) The SAWs generated by the focused interdigital transducers (FIDTs) leak at the substrate–oil interface and induce acoustic streaming in the chamber. (c) Micrograph of the acoustofluidic droplet dispensing structure. The orifice locates at the focal point of the FIDTs (shown as the triangular alignment mark in this micrograph). (d) Schematic of a droplet package in (a). Droplets are dispensed successively in end-to-end droplet packages. As a protocol, each package consists of an "Interpackage Gap Droplet" (a large droplet) to indicate the beginning of a package, a 3-bit "Address Bit Droplets" of the package (three droplets with regulated sizes) to present the binary address of the package by volume, and five "Sample Bit Droplets" with consistent volume. Based on this setup, each droplet sample is assigned to a specific identification number consisting of a package address and a sequence number in this package. The five droplet samples here are represented by identification numbers "001-1", "001-2", …, "001-5", respectively.

into independent end-to-end droplet packages. As a proof-of-concept demonstration, in this work, a package consists of one "Interpackage Gap Droplet", three "Address Bit Droplets", and five "Sample Bit Droplets". More specifically, the "Interpackage Gap Droplet" separates two adjacent droplet packages and denotes the start of a package. The "Interpackage Gap Droplet" large volume helps the identification accuracy between packages. The volume of the following "Address Bit Droplets" is tuned to be either address bit "0" (smaller ones) or address bit "1" (larger ones). Thus, arranged in binary by volume, three droplets present the three-bit address code of the package (increasing from "0" "0" "0" to "1" "1" "1"). The following monodispersed "Sample Bit Droplets" could be used as independent micro-reactors for single cell-cultivation, compound screening, drug screening, and emulsion PCR.

Consequently, every sample droplet is assigned to a specific identification number combined by a package address code and a sequence number in the package. As the schematic illustrated in Fig. 1d, the binary address code of the package is "001" while the identification numbers of five "Sample Bit Droplets" increase from "001-1" to "001-5".

On-demand droplet dispensing

The droplet dispensing process is demonstrated by Fig. 2. The flow rates of water and oil are 4.5 μL min^{-1} and 5 μL min^{-1}, respectively. Actuated by a 5 ms TSAW pulse, the induced oil jet splits the water flow and forms a droplet. To achieve a robust interface between oil and water, the flow rates of the two-phase fluids were tuned separately to determine the optimal conditions for distinct phases. The influence of flow rates on the stability of the oil–water interface was characterized at a dispensing speed of 100 drops per second (*i.e.*, pulse width: 5 ms, interval: 5 ms). As shown in Fig. 3, a stable oil–water interface is formed at the orifice of the chamber and the two-phase flows are in separate paths without interfering with each other (as shown

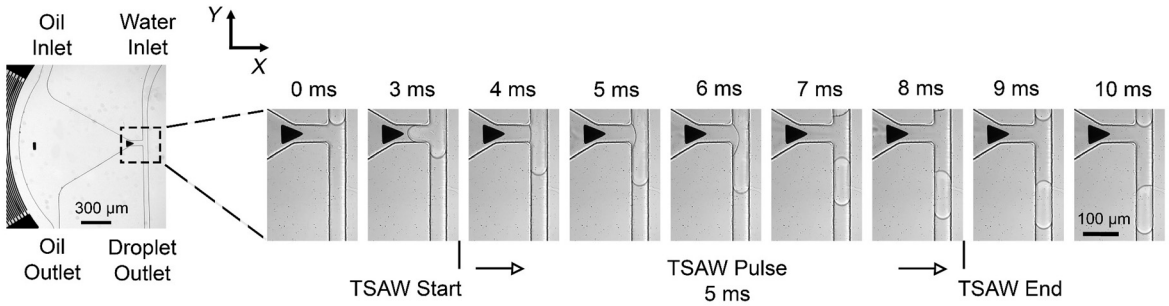

Fig. 2 Micrographs of acoustofluidic droplet dispensing process. The oil flow was jetted from the chamber under the effect of TSAWs, which cuts the water flow off to form a droplet downstream of the T-junction. The flow rates of water and oil are 4.5 μL min^{-1} and 5 μL min^{-1}, respectively. The duration of the TSAW pulse is 5 ms. The gap period between adjacent pulses is 5 ms.

by grey squares in Fig. 3). When the oil flow rate is too large, the oil will be pushed out through the orifice into the water channel even without the excitation of TSAW (*i.e.*, the diamond marks in red). In contrast, when the water flow rate is too large, the water flows into the oil chamber through the orifice (*i.e.*, the circle marks in blue). Flow rate combinations suitable for the stable and sustainable dispensing process are noted by the grey solid symbols in Fig. 3. For droplet dispensing frequency higher than 100 Hz, the volume variation of sustainable dispensed droplets increases significantly, which increases the potential for coding errors. To achieve accurate dispensing at a higher frequency, one can reduce the width of the microchannel or increase the actuation voltage. In this work, the highest dispensing frequency used in experiments is 100 Hz. The volumes of droplets dispensed at a 100 Hz frequency were measured while changing the flow rates of oil and water (Fig. 4). As shown in Fig. 4, the droplet size increases proportionally to the water flow rate.

In addition, a series of experiments have been conducted to characterize the influence of the pulse intervals of TSAWs on a droplet's volume (Fig. 5). Given that the water is pumped into the microchannel at a constant flow rate in the dispensing process, the volumes of the dispensed water droplets are proportional to the pulse intervals, which is consistent with our experimental observations.

More specifically, the droplet size is determined by the length of water flow extruded beyond the orifice for droplet splitting, which accounts for the linearity to the measured data in Fig. 4 and 5a. This has been confirmed by the fact that the slopes of each linear model matches with the flow rate of water under specific pulse durations. This feature suggests that by programming the intervals of TSAW pulses, the volumes of continuously dispensed droplets could be

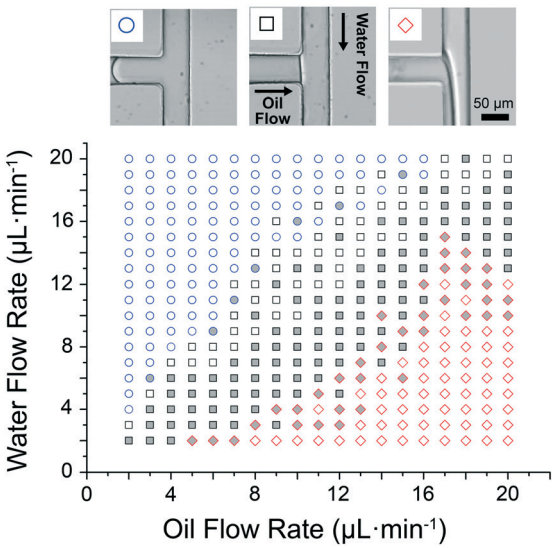

Fig. 3 Influence of flow rates on the dispensing stability. When the flow rates of water and oil are balanced, the interface at the orifice is stable and two streams flow *via* corresponding paths (black square). If the flow rate of the oil stream becomes large enough, it will be pushed out through the orifice into the water channel (red diamond). When the water flow rate is too large to maintain the stable water–oil interface, the water flows into the oil chamber (blue circle). Combinations of flow rates suitable for the dispensing process actuated by 5 ms width TSAW at a frequency of 100 Hz is denoted by the grey fillings. The scale bar is 50 μm.

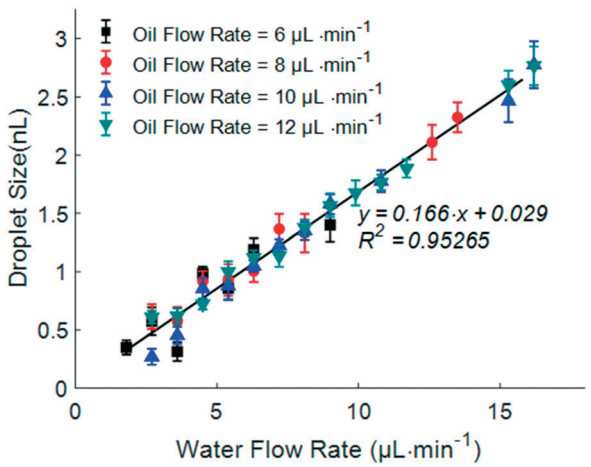

Fig. 4 Effect of the flow rate on the acoustofluidic droplet dispensing process. In our design, the dispersed droplet size is proportional to the water flow rate but independent of the oil flow rate. Each period of the acoustic pulse consists of a 5 ms TSAW pulse and a 5 ms rest period. Each point in this figure is averaged over 5 tests, and each test 6–8 droplets.

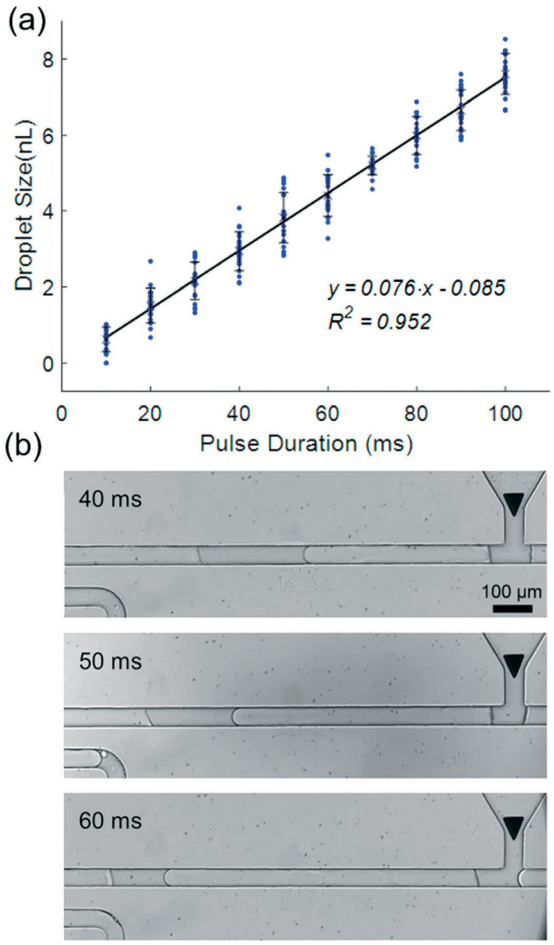

Fig. 5 Effect of the pulse interval on droplet dispensing. (a) The volume of dispensed droplets as a function of the pulse period. In our experiments, each pulse period consists of a 5 ms TSAW pulse and a rest period before the next pulse. The pulse period can be tuned by varying the duration of the gap period. The flow rates of water and oil are 4.5 μL min^{-1} and 5 μL min^{-1}, respectively. The results are averaged over 5 tests, with each test having 5 droplets. (b) Micrographs of dispensed droplets with 40 ms, 50 ms, and 60 ms pulse intervals.

controlled on-demand (ESI† Note S2, Fig. S2 and S3), leading to the potential of encoding readable texts to the droplet sequences (Fig. S2,† 'DUKE' encoded with Morse code).

The long-term operation of acoustofluidic droplet coding unit is primarily limited by the pumping methods of water. The time-averaged droplet generation speed needs to match with the constant flow rate of water in long-term operations, otherwise the coding unit will experience unexpected time-cumulative pressure biases which leads to periodical coding errors. However, such issues can be mediated by error recovery methods or eliminated by pumping with constant pressure pumps. Under current experimental setup, the droplet generation process can be maintained for 2 min at 20 Hz with time-lapsed volume distribution of the first 37.55 s shown in Fig. S4.† Notably, the rate of generating abnormal droplets (of which volumes are beyond 2 standard deviation) increases from 3.5% to above 8% after the first 11.65 seconds. Fig. S5† shows recorded volumes of droplets continuously generated at 20 Hz over the first 30 seconds since the SAW was on. The distribution of droplet volumes has a mean value of 1.66 nL (which matches with the water flowrate of 2 μL min^{-1}) and a stand deviation of 0.25 nL.

Droplet coding

Typically, the barcoding and identification of a large number of droplets is a complicated process in microfluidic systems. Herein, based on the functionality demonstrated above, we utilize our acoustofluidic-based on-demand droplet dispensing approach to achieve real-time, on-demand droplet coding by programming the pulse intervals in a sequence of TSAW bursts.

Fig. 6 demonstrates the proof-of-concept droplet coding functionality based on our platform. The flow rates of water and oil are 4.5 μL min^{-1} and 5 μL min^{-1}, respectively. The volumes of "Sample Bit Droplets", "Address Bit Droplets" – "0", "Address Bit Droplets" – "1", and "Interpackage Gap Droplets" are 0.75 nL, 1.5 nL, 3 nL, and 4.5 nL, corresponding to gap periods of 5 ms, 15 ms, 35 ms, and 55 ms, respectively, for the acoustic pulse. Each package consists of a long droplet, three droplets with modulated sizes, and five small droplets of a monodispersed size distribution. The capacity of this package address code can be greatly expanded by either using more binary "Address Bit Droplets" or by switching to a decimal address code by refining the size changes between address droplets. The sample capacity of each package can be increased by containing more "Sample Bit Droplets", while their small size ensures the throughput of the dispensing process. The related discussions on the upper droplet coding limit is enclosed in ESI† Note S4.

Based on this setup, each droplet is assigned to a specific identification number consisting of a package address code and a sequence number in the package. This greatly simplifies the identification of a target droplet from a colossal number of droplets. For example, the identification number of the 20th droplet in a droplet sequence is "011-5" (the 5th droplet in the "011" droplet package) in our protocol as demonstrated by the droplet in the red dashed square box in Fig. 6a. To find this droplet, we only need to first identify the address code of this package and then find out the 5th sample droplet in the package. The identification of droplets can be carried out with a microscope or other detection methods with the ability to identify the size of droplets. Moreover, for two adjacent droplet packages, the address code of the later generated package should increase by 1 in binary compared to the first generated one. This feature helps the detection of coding errors and increases the fault tolerance of the droplet identification process. The related discussions on error recovery is enclosed in ESI† Note S5. Conclusively, our droplet coding technique presents a programmable and easy-to-fabricate approach for the deterministic generation of droplets based on their sizes and serial arrangements in microfluidic systems.

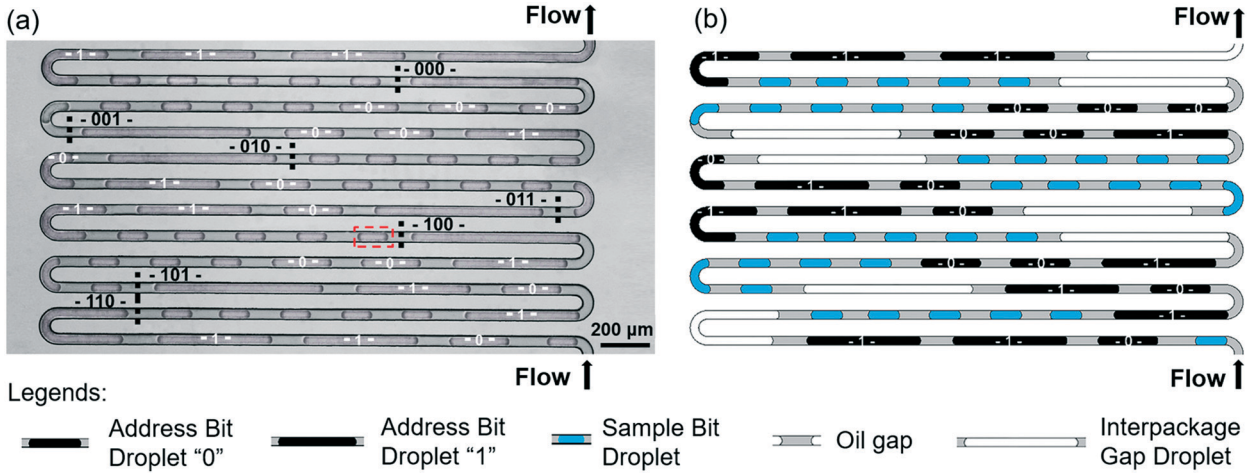

Fig. 6 A proof-of-concept protocol for acoustofluidic droplet coding. (a) Micrograph and (b) schematic of the encoded droplet array. Herein, droplets are dispensed successively in end-to-end droplet packages. Each package consists of a large droplet, three droplets with regulated sizes, and five small droplets of monodispersed size, which work as an interpackage gap to denote the start of a droplet package, address bits to give the binary address code of the package by volume, and droplet samples, respectively. Thus, each droplet sample in this sequence is assigned to a unique identifier code with an address code of the package it belongs to and its sequence number in this package. For example, as shown by the dashed red box, the droplet is assigned to an identifier 011-5, which represents the 5th droplet in the package with an address code 011. The capacity of this coding approach can be greatly expanded by using more droplets for the address bit or by increasing the number of sample droplets in one package.

Materials and methods

Device fabrication

As the schematic shows in Fig. 1, the platform we employed mainly consists of two components: (1) a microchannel layer formed with polydimethylsiloxane (PDMS), and (2) a double-side polished 128° *Y*-cut, *X*-propagating lithium niobate ($LiNbO_3$) substrate with a 60° circular FIDT patterned on its surface. 10 nm chrome/200 nm gold FIDTs were patterned on $LiNbO_3$ substrates with standard photolithography using SPR3012 photoresist (MicroChem, USA) and an e-beam evaporation and lift-off process. The finger width and spacing are 10 μm, resulting in a designed resonance frequency of about 96.25 MHz. The detailed dimensions of the FIDT design are shown in Fig. S6.† The mold for the microchannel network was fabricated by standard photolithography using SU-8 100 photoresist (MicroChem, USA) on a single-side polished silicon wafer. PDMS base and cross-linker (Sylgard 184, Dow Corning, USA) were mixed at a ratio of 10 : 1 (w/w), poured onto the SU-8 mold, and then cured at 65 °C for two hours. Afterwards, the cured PDMS module was peeled away from the silicon wafer and punched at predesignated positions to enable sample loading and unloading. The width and height of the water microchannel are 50 μm and 100 μm, respectively. After modifying the PDMS surface with (3-aminopropyl)triethoxysilane (Sigma-Aldrich, USA) and treated with oxygen plasma, the PDMS channel and the $LiNbO_3$ substrate were bonded together and then incubated at 65 °C overnight.

Experimental setup

Deionized water and oil (Fluorinert™ FC-40, Sigma-Aldrich, USA) were injected into the microchannel by a syringe pump (neMESYS, Germany). The oil fluid was stabilized by 0.2% (w/w) surfactant (008-FluoroSurfactant, RAN Biotechnologies, USA). AC signal generated by a function generator (E4400B, Agilent Technologies, USA) was amplified by an amplifier (25A250A, Amplifier Research, USA) and then transmitted into the FIDTs at 150 Vpp. Before tests, we used a network analyzer (Vector Network Analyzer 2180, Array Solutions, USA) and observations under the microscope to identify the strongest acoustic streaming intensity, and an optimal actuation frequency of 96.25 MHz was chosen for the platform. Images and videos of the dispensing process were captured by a fast camera (FastCam SA4, Photron, USA) through Photron FASTCAM Viewer (PFV, Photron, USA) using a microscope (TE2000-U, Nikon, Japan).

Droplet measurement

Similar to previous publications on droplet microfluidics,[59–61] we estimate the volume of the droplet by multiplying the length of droplet by the cross-sectional area of channel (50 μm × 100 μm). The lengths of droplet are obtained by measuring the distances of the two lateral midpoints of the two curvatures on the end of droplets. Due to the defects in microfabrication, the width and height of the serpentine channel are not consistent, which will lead to ~1% inconsistency on volume measurements from droplet to droplet. The measurement pipeline has recently been automated using imaging processing algorithms (ESI† Note S5 and Movie S4).

Discussions and conclusions

The accurate and high-throughput identification of the target droplet among a series of flowing droplets is necessary, but

still challenging. Conventional coding methods for a large number of droplet samples have suffered from their complicated preparation processes, low level of automation, and difficulties in the visualization of decoding results. Here, we demonstrate that acoustofluidics enabled on-demand regulation of the droplet size and deterministic coding of a droplet sequence by the spatial arrangement. Compared to existing droplet coding techniques relying on extra labels, our strategy encodes information in the serial combinations of droplet volumes and thus holds tremendous coding capacity as well as potentials in error recovery. This is advantageous for the screening of single-cell kinetics since the colossal numbers of heterogeneous responses of single cells over a long time will easily exceed the coding and decoding capacities by existing barcoding techniques. Also, when dealing with multiplexed testing reagents and conditions, our coding strategy can encode the corresponding testing parameters to the 'address bits' in real-time, granting users the capability to pin-point individual micro-beakers in either on-chip monitoring or downstream operations, which is further discussed in ESI† Note S6. Although advantageous, the tradeoff is the generated droplet trains have to be kept in a serial format to maintain the encoded information, suggesting the droplets need to be incubated in a serpentine channel or a long tube. Conclusively, the acoustofluidic droplet dispensing device presented here allows dynamic regulation of droplet volumes in high-speed flow and deterministic information coding, which can potentially lead to applications such as deterministic single cell barcoding and screening.

Author contributions

P. Zhang, W. Wang, and T. J. Huang designed the project. W. Wang and P. Zhang carried out the experiments. H. Fu helped fabricating the controlling module of the function generator. J. Xia worked on the simulation. W. Wang, P. Zhang, H. Bachman, J. Zhou and T. J. Huang discussed the results, co-wrote the manuscript. P. Zhang, W. Wang, J. Rich, J. Zhou, and T. J. Huang revised the manuscript.

Conflicts of interest

T. J. H. has co-founded a start-up company, Ascent Bio-Nano Technologies Inc., to commercialize technologies involving acoustofluidics and acoustic tweezers.

Acknowledgements

This work was supported by the National Institutes of Health (R01GM132603, R01GM135486, UG3TR002978, R33CA223908, R01GM127714, and R01HD086325), National Science Foundation (ECCS-1807601), the National Natural Science Foundation of China with Grant No. 61874033, the Natural Science Foundation of Shanghai Municipal Government with Grant No. 18ZR1402600, and the State Key Lab of ASIC and System, Fudan University with Grant No. 2018MS003.

References

1 D. Geißler, L. J. Charbonnière, R. F. Ziessel, N. G. Butlin, H. G. Löhmannsröben and N. Hildebrandt, *Angew. Chem., Int. Ed.*, 2010, **49**, 1396–1401.
2 S. H. Jin, S. C. Jang, B. Lee, H. H. Jeong, S. G. Jeong, S. S. Lee, K. P. Kim and C. S. Lee, *Lab Chip*, 2016, **16**, 1358–1365.
3 L. Dong, D. W. Chen, S. J. Liu and W. Du, *Sci. Rep.*, 2016, **6**, 24192.
4 M. Courtney, X. Chen, S. Chan, T. Mohamed, P. P. N. Rao and C. L. Ren, *Anal. Chem.*, 2017, **89**, 910–915.
5 J. Clausell-Tormos, A. D. Griffiths and C. A. Merten, *Lab Chip*, 2010, **10**, 1302–1307.
6 F. Eduati, R. Utharala, D. Madhavan, U. P. Neumann, T. Longerich, T. Cramer, J. Saez-Rodriguez and C. A. Merten, *Nat. Commun.*, 2018, **9**, 2434.
7 Z. Chen, P. Liao, F. Zhang, M. Jiang, Y. Zhu and Y. Huang, *Lab Chip*, 2017, **17**, 235–240.
8 F. Schuler, M. Trotter, M. Geltman, F. Schwemmer, S. Wadle, E. Domínguez-Garrido, M. López, C. Cervera-Acedo, P. Santibáñez, F. Von Stetten, R. Zengerle and N. Paust, *Lab Chip*, 2016, **16**, 208–216.
9 L. J. Wang, R. Sun, T. Vasile, Y. C. Chang and L. Li, *Anal. Chem.*, 2016, **88**, 8302–8308.
10 G. Xu, D. Nolder, J. Reboud, M. C. Oguike, D. A. van Schalkwyk, C. J. Sutherland and J. M. Cooper, *Angew. Chem., Int. Ed.*, 2016, **55**, 15250–15253.
11 Y. Leng, K. Sun, X. Chen and W. Li, *Chem. Soc. Rev.*, 2015, **44**, 5552–5595.
12 G. MacBeath and S. L. Schreiber, *Science*, 2000, **289**, 1760–1763.
13 Y. Zhang, J. Sun, Y. Zou, W. Chen, W. Zhang, J. J. Xi and X. Jiang, *Anal. Chem.*, 2015, **87**, 900–906.
14 T. F. Scherr, S. Gupta, D. W. Wright and F. R. Haselton, *Lab Chip*, 2017, **17**, 1314–1322.
15 M. Yang, W. Zhang, W. Zheng, F. Cao and X. Jiang, *Lab Chip*, 2017, **17**, 3874–3882.
16 S. Wu, C. Li, H. Shi, Y. Huang and G. Li, *Anal. Chem.*, 2018, **90**, 9929–9935.
17 G. K. Geiss, R. E. Bumgarner, B. Birditt, T. Dahl, N. Dowidar, D. L. Dunaway, H. P. Fell, S. Ferree, R. D. George, T. Grogan, J. J. James, M. Maysuria, J. D. Mitton, P. Oliveri, J. L. Osborn, T. Peng, A. L. Ratcliffe, P. J. Webster, E. H. Davidson and L. Hood, *Nat. Biotechnol.*, 2008, **26**, 317–325.
18 Y. Li, Y. T. H. Cu and D. Luo, *Nat. Biotechnol.*, 2005, **23**, 885–889.
19 A. Agrawal, R. Deo, G. D. Wang, M. D. Wang and S. Nie, *Proc. Natl. Acad. Sci. U. S. A.*, 2008, **105**, 3298–3303.
20 X. Li, T. Wang, J. Zhang, D. Zhu, X. Zhang, Y. Ning, H. Zhang and B. Yang, *ACS Nano*, 2010, **4**, 4350–4360.
21 J. A. Lee, S. Mardyani, A. Hung, A. Rhee, J. Klostranec, Y. Mu, D. Li and W. C. W. Chan, *Adv. Mater.*, 2007, **19**, 3113–3118.
22 S. Sattayasamitsathit, J. Burdick, R. Bash, P. Kanatharana, P. Thavarungkul and J. Wang, *Anal. Chem.*, 2007, **79**, 7571–7575.

23 Y. Xiang, Y. Zhang, Y. Chang, Y. Chai, J. Wang and R. Yuan, *Anal. Chem.*, 2010, **82**, 1138–1141.
24 S. Rauf, A. Glidle and J. M. Cooper, *Chem. Commun.*, 2010, **46**, 2814–2816.
25 U. K. Demirok, J. Burdick and J. Wang, *J. Am. Chem. Soc.*, 2009, **131**, 22–23.
26 K. A. White, D. A. Chengelis, K. A. Gogick, J. Stehman, N. L. Rosi and S. Petoud, *J. Am. Chem. Soc.*, 2009, **131**, 18069–18071.
27 Y. Zhang, L. Zhang, R. Deng, J. Tian, Y. Zong, D. Jin and X. Liu, *J. Am. Chem. Soc.*, 2014, **136**, 4893–4896.
28 Y. Zhao, H. C. Shum, H. Chen, L. L. A. Adams, Z. Gu and D. A. Weitz, *J. Am. Chem. Soc.*, 2011, **133**, 8790–8793.
29 L. S. Lawson and J. D. Rodriguez, *Anal. Chem.*, 2016, **88**, 4706–4713.
30 F. Hu, C. Zeng, R. Long, Y. Miao, L. Wei, Q. Xu and W. Min, *Nat. Methods*, 2018, **15**, 194–200.
31 K. Kamil Reza, J. Wang, R. Vaidyanathan, S. Dey, Y. Wang and M. Trau, *Small*, 2017, **13**, 1602902.
32 L. Wu, Z. Wang, K. Fan, S. Zong and Y. Cui, *Small*, 2015, **11**, 2798–2806.
33 S. Brakmann, *Angew. Chem., Int. Ed.*, 2004, **43**, 5730–5734.
34 S. S. Agasti, M. Liong, V. M. Peterson, H. Lee and R. Weissleder, *J. Am. Chem. Soc.*, 2012, **134**, 18499–18502.
35 F. Lan, J. R. Haliburton, A. Yuan and A. R. Abate, *Nat. Commun.*, 2016, **7**, 11784.
36 H. Lee, J. E. Park and J. M. Nam, *Nat. Commun.*, 2014, **5**, 3367.
37 A. M. Klein, L. Mazutis, I. Akartuna, N. Tallapragada, A. Veres, V. Li, L. Peshkin, D. A. Weitz and M. W. Kirschner, *Cell*, 2015, **161**, 1187–1201.
38 A. S. Utada, E. Lorenceau, D. R. Link, P. D. Kaplan, H. A. Stone and D. A. Weitz, *Science*, 2005, **308**, 537–541.
39 P. B. Umbanhowar, V. Prasad and D. A. Weitz, *Langmuir*, 2000, **16**, 347–351.
40 T. Thorsen, R. W. Roberts, F. H. Arnold and S. R. Quake, *Phys. Rev. Lett.*, 2001, **86**, 4163–4166.
41 A. R. Abate, P. Mary, V. Van Steijn and D. A. Weitz, *Lab Chip*, 2012, **12**, 1516–1521.
42 P. Garstecki, M. J. Fuerstman, H. A. Stone and G. M. Whitesides, *Lab Chip*, 2006, **6**, 437–446.
43 T. Ward, M. Faivre, M. Abkarian and H. A. Stone, *Electrophoresis*, 2005, **26**, 3716–3724.
44 P. Garstecki, H. A. Stone and G. M. Whitesides, *Phys. Rev. Lett.*, 2005, **94**, 164501.
45 Y. H. Lin, C. H. Lee and G. Bin Lee, *J. Microelectromech. Syst.*, 2008, **17**, 573–581.
46 S. L. Anna, N. Bontoux and H. A. Stone, *Appl. Phys. Lett.*, 2003, **82**, 364–366.
47 J. Friend and L. Y. Yeo, *Rev. Mod. Phys.*, 2011, **83**, 647–704.
48 R. Barnkob, N. Nama, L. Ren, T. J. Huang, F. Costanzo and C. J. Kähler, *Phys. Rev. Appl.*, 2018, **9**, 014027.
49 Z. Tian, S. Yang, P. H. Huang, Z. Wang, P. Zhang, Y. Gu, H. Bachman, C. Chen, M. Wu, Y. Xie and T. J. Huang, *Sci. Adv.*, 2019, **5**, eaau6062.
50 Z. Tian, Z. Wang, P. Zhang, T. D. Naquin, J. Mai, Y. Wu, S. Yang, Y. Gu, H. Bachman, Y. Liang, Z. Yu and T. J. Huang, *Sci. Adv.*, 2020, **6**, eabb0494.
51 M. Wu, Y. Ouyang, Z. Wang, R. Zhang, P. H. Huang, C. Chen, H. Li, P. Li, D. Quinn, M. Dao, S. Suresh, Y. Sadovsky and T. J. Huang, *Proc. Natl. Acad. Sci. U. S. A.*, 2017, **114**, 10584–10589.
52 R. Mikhaylov, F. Wu, H. Wang, A. Clayton, C. Sun, Z. Xie, D. Liang, Y. Dong, F. Yuan, D. Moschou, Z. Wu, M. H. Shen, J. Yang, Y. Fu, Z. Yang, C. Burton, R. J. Errington, M. Wiltshire and X. Yang, *Lab Chip*, 2020, **20**, 1807–1814.
53 M. Wu, A. Ozcelik, J. Rufo, Z. Wang, R. Fang and T. Jun Huang, *Microsyst. Nanoeng.*, 2019, **5**, 32.
54 M. Wu, Z. Mao, K. Chen, H. Bachman, Y. Chen, J. Rufo, L. Ren, P. Li, L. Wang and T. J. Huang, *Adv. Funct. Mater.*, 2017, **27**, 1606039.
55 J. Zhang, S. Yang, C. Chen, J. H. Hartman, P. H. Huang, L. Wang, Z. Tian, P. Zhang, D. Faulkenberry, J. N. Meyer and T. J. Huang, *Lab Chip*, 2019, **19**, 984–992.
56 T. Franke, A. R. Abate, D. A. Weitz and A. Wixforth, *Lab Chip*, 2009, **9**, 2625–2627.
57 L. Schmid, D. A. Weitz and T. Franke, *Lab Chip*, 2014, **14**, 3710–3718.
58 L. Schmid and T. Franke, *Lab Chip*, 2013, **13**, 1691–1694.
59 J. H. Jung, G. Destgeer, B. Ha, J. Park and H. J. Sung, *Lab Chip*, 2016, **16**, 3235–3243.
60 M. Sesen, C. Devendran, S. Malikides, T. Alan and A. Neild, *Lab Chip*, 2017, **17**, 438–447.
61 J. C. Brenker, D. J. Collins, H. Van Phan, T. Alan and A. Neild, *Lab Chip*, 2016, **16**, 1675–1683.
62 S. P. Zhang, J. Lata, C. Chen, J. Mai, F. Guo, Z. Tian, L. Ren, Z. Mao, P. H. Huang, P. Li, S. Yang and T. J. Huang, *Nat. Commun.*, 2018, **9**, 2928.
63 J. T. Luo, N. R. Geraldi, J. H. Guan, G. McHale, G. G. Wells and Y. Q. Fu, *Phys. Rev. Appl.*, 2017, **7**, 014017.
64 D. J. Collins, T. Alan, K. Helmerson and A. Neild, *Lab Chip*, 2013, **13**, 3225–3231.
65 P. Zhang, C. Chen, X. Su, J. Mai, Y. Gu, Z. Tian, H. Zhu, Z. Zhong, H. Fu, S. Yang, K. Chakrabarty and T. J. Huang, *Sci. Adv.*, 2020, **6**, eaba0606.
66 A. Ozcelik, J. Rufo, F. Guo, Y. Gu, P. Li, J. Lata and T. J. Huang, *Nat. Methods*, 2018, **15**, 1021–1028.

